ECOLOGY

A continent-wide assessment of the form and intensity of large mammal herbivory in Africa

Gareth P. Hempson,[1,2]* Sally Archibald,[2] William J. Bond[1,3]

Megafaunal extinctions and a lack of suitable remote sensing technology impede our understanding of both the ecological legacy and current impacts of large mammal herbivores in the Earth system. To address this, we reconstructed the form and intensity of herbivory pressure across sub-Saharan Africa ~1000 years ago. Specifically, we modeled and mapped species-level biomass for 92 large mammal herbivores using census data, species distributions, and environmental covariates. Trait-based classifications of these species into herbivore functional types, and analyses of their biomass surfaces, reveal four ecologically distinct continental-scale herbivory regimes, characterized by internally similar forms and intensities of herbivory pressure. Associations between herbivory regimes, fire prevalence, soil nutrient status, and rainfall provide important insights into African ecology and pave the way for integrating herbivores into global-scale studies.

The past 15 years have witnessed a revolution in our understanding of how fire shapes ecosystems at global scales (*1*–*4*). However, the relevance of another major consumer of vegetation, the large mammalian herbivores, has been largely neglected. This is in part because remote sensing tools, such as the Moderate Resolution Imaging Spectroradiometer (MODIS), provide near-daily global data sets that allow fire extent, frequency, and intensity to be quantified at 250-m resolution (*5*, *6*); equivalent tools are not available for directly quantifying herbivore community composition and biomass. An important application of the well-developed understanding of fire at macroscales has been its implementation in Dynamic Global Vegetation Models (DGVMs). These global models allow researchers to explore the implications of global climate change for fire regimes and the concomitant impacts on global vegetation patterns and Earth system feedbacks (*7*–*10*). Looking backward in time, an understanding of climate–vegetation–fire relationships also allows reconstruction of the environmental contexts that have shaped biotic evolutionary trajectories (*11*–*13*). Like fire, large herbivores can have a substantial impact on the structure and function of ecological communities (*14*–*18*), and past alterations in the composition and degree of mammalian herbivory (e.g., Pleistocene megafaunal extinctions) have affected global vegetation and Earth system

processes (*19*–*22*). There is thus an urgent need to develop tools that explore how the biotic interactions of herbivores and other consumers have shaped current and past ecological function, processes, and resilience across global ecosystems (*23*–*25*).

Early ecologists organized the diverse vegetation on Earth into biomes, or global vegetation units that internally share similar vegetation functional traits and respond in the same way to environmental drivers (*26*, *27*). Plant functional types form the basis of these classifications by simplifying vast species-level diversity into groups based on common biological attributes (e.g., deciduous versus evergreen trees) (*28*–*30*). More recently, access to global-scale information about fire has enabled the delineation of global fire regimes, or "pyromes," parts of the globe grouped by their shared fire characteristics and responses to environmental change (*31*). Key to both of these classification systems is the assessment of syndromes of plant functional types or fire characteristics that, because of energetic or environmental constraints, tend to occur together. This categorization can be useful in assessing how the distributions of biomes and pyromes might change in response to environmental change, and how closely linked fire regimes and vegetation distributions are. Using the same approach to assess global syndromes of herbivory can inform the understanding of interactions between herbivores and other components of the Earth system.

Determining large-scale herbivory patterns

We reconstructed herbivore biomass surfaces across sub-Saharan Africa for 92 large mammal herbivore species, using statistical models fitted to census data from protected areas. Rainfall, soil

nutrient status, and vegetation patterns were fitted as covariates and used to predict species' biomass across their distribution range, which was then refined by fine-scale habitat preferences (figs. S1 and S2 and tables S1 and S2) (*32*). Our aim was to quantify herbivore biomass before human hunting with guns, and thus potential herbivory surfaces, ~1000 years ago. Data availability and model fit determined whether species densities (individuals/km²) were modeled (using analysis of covariance) at (i) vegetation group level (forest, caesalpinioid savanna, mixed savanna, grassland, or shrubland) or (ii) across their full distribution range. Alternately, median densities were applied at (iii) vegetation group or (iv) overall levels; otherwise, (v) an expert opinion estimate was applied. Elephant density estimates were based on 95th-quantile regression to account for reduced current-day densities, which are due to their large home ranges exceeding the extent of protected areas and considerable current and historical hunting pressure. Species densities were reduced to 10 or 0% of predicted values for low-suitability or unsuitable habitats and converted to biomass (kg/km²) using average adult body mass. This analysis provides the first large-scale mapped information on wild herbivore biomass [although the United Nations Food and Agriculture Organization (FAO) has produced spatial data on livestock densities for several continents] (Fig. 1). Previous similar studies have fitted species- (*33*) and community-level (*34*–*36*) regression equations relating biomass to rainfall and soil nutrient status [(*37*) analyzes large herbivore diversity patterns]. These studies restricted their focus to large mammal herbivores in the savanna biome and did not attempt to create spatial biomass surfaces.
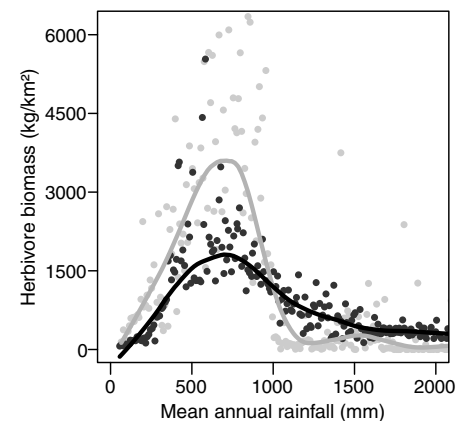
Fig. 1. Relationships between African herbivore biomass and rainfall. Reconstructed historical total wildlife biomass (black points and black line) and current FAO livestock biomass estimates (gray points and gray line) are shown in relation to rainfall. Elephants overwhelm the signal from the other species and are excluded from the figure. Points represent median values for 10-mm rainfall intervals and are shown with locally weighted scatterplot smoothing regression lines.

[1]Department of Biological Sciences, University of Cape Town, Private Bag X1, Rondebosch, 7701, South Africa. [2]School of Animal, Plant and Environmental Sciences, University of the Witwatersrand, Wits, 2050, South Africa. [3]South African Environmental Observation Network, care of the Department of Biological Sciences, University of Cape Town, Private Bag X1, Rondebosch, 7701, South Africa.
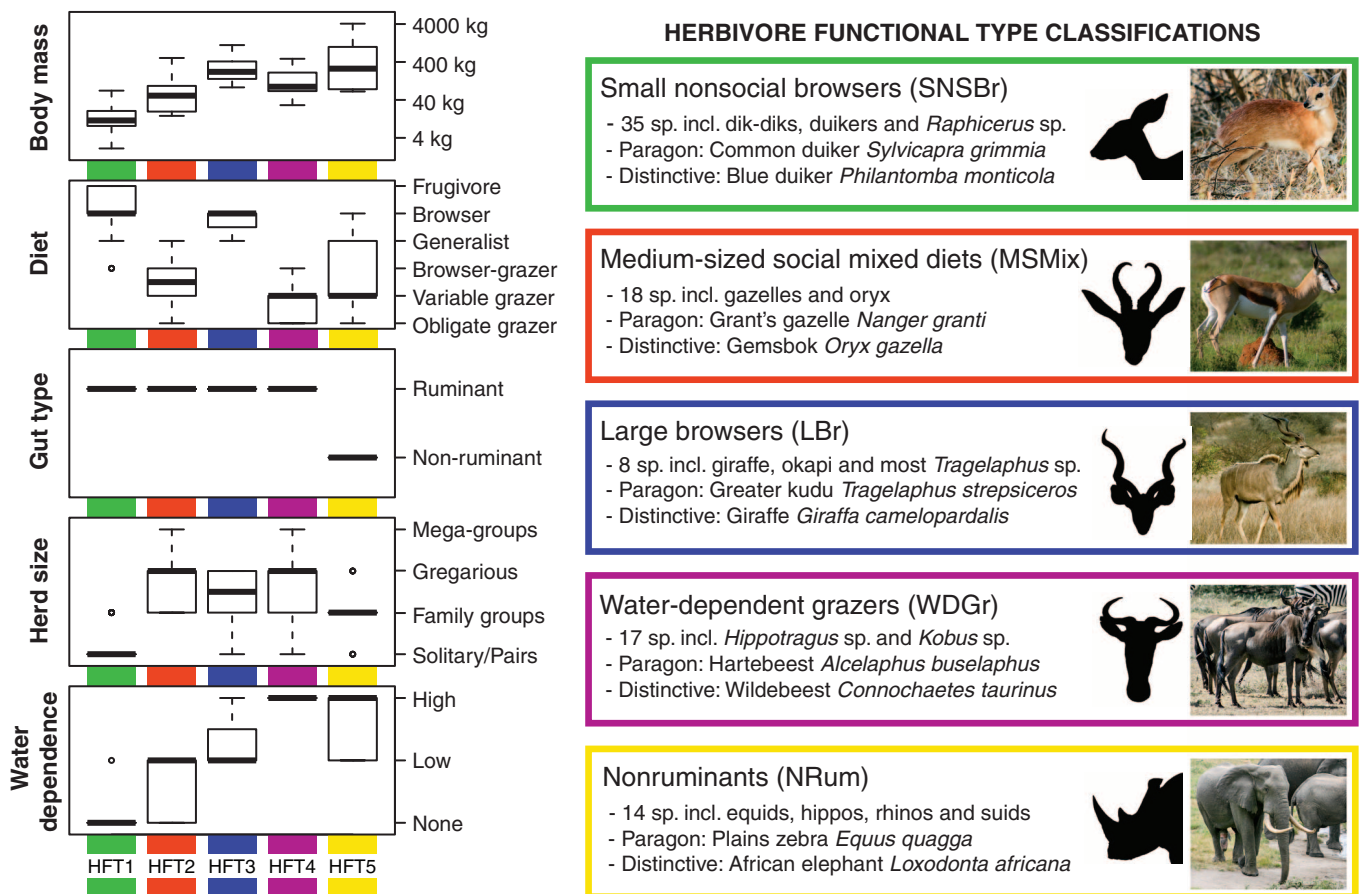*Corresponding author. E-mail: ghempson@gmail.com

We reduced species-level complexity by trait-based classifications of species into herbivore functional types (HFTs), analogous to grass, shrubs, and trees in a vegetation context. Hierarchical cluster analysis was used to partition species into HFTs based on five traits: body mass, diet, gut type, herd size, and water dependence (see Fig. 2 and tables S3 and S4 for detailed trait information). These traits are important for understanding consumption patterns in terms of the amount (body mass and gut type), type (diet and gut type), and spatial patterning (herd size and water dependence) of forage offtake. Furthermore, in a tropical and subtropical African context, these traits largely capture the forage resource and habitat characteristics of species (including thermal tolerance) that will shape their responses to global environmental changes. Our HFT classifications should thus prove useful for populating DGVMs with large mammal herbivores (38). HFT biomass surfaces were created by combining species-level biomass surfaces, enabling each 1° grid square (~12,000 km^2 at the equator) to be characterized by its total herbivore biomass (kg/km^2) and that of each HFT. Gro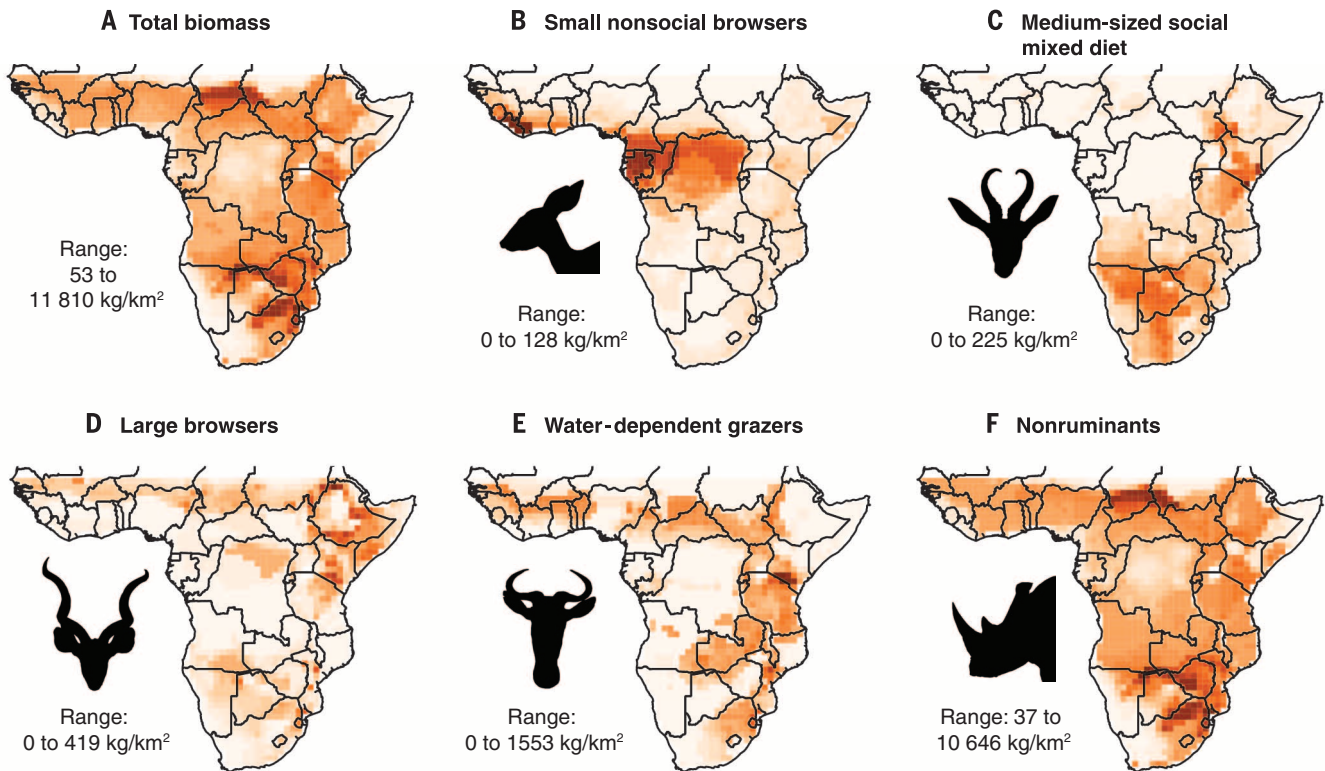uping 1° squares with similar herbivore biomass characteristics using cluster analyses allows delimitation of different large mammal herbivory regimes, or "herbivomes," analogous to biome and pyrome classifications. These large-scale patterns in the relative abundance of HFTs and total herbivore biomass show how the form and intensity of consumptive offtake by large mammal herbivores vary across sub-Saharan Africa.

Biomass surfaces

Elephants dominate African herbivore biomass, often having biomasses equivalent to those of all other species combined (fig. S3). Excluding elephants, which obscure biomass patterns, reveals a unimodal relationship between potential African mammal herbivore biomass and mean annual rainfall (MAR), peaking at ~1700 kg/km^2 and ~700 mm MAR (Fig. 1). This finding contrasts with previous studies that report a constant linear increase in the log biomass–log MAR relationship from ~150 to 1200 mm (33–35), implying an accelerating increase in herbivore biomass gain with MAR. Our analyses include data from these earlier studies, and disparities are attributable to differences in spatial resolution, our incorporation of vegetation attributes and habitat preference, and the sensitivity of their analyses to biomass declines at high rainfalls when analyzing log-transformed data. The general functional form of our biomass-rainfall curve is in close agreement with present-day estimates of livestock biomass (www.fao.org). Peak densities of livestock are almost two times higher between 500 and 750 mm MAR [perhaps reflecting management interventions such as the provision of drinking water and supplemental feed and the suppression of disease and predation (39)], but modeled precolonial wildlife densities are higher above 1000 mm MAR. The inclusion of elephant biomass predictions further increases the disparity between wildlife and livestock biomass at high rainfall. An elephant's massive body size and mixed diet enable effective utilization of diverse and even low-quality forage typical of high-rainfall areas, and elephants thus exhibit a lack of response to soil nutrient status and vegetation composition (14). This is reflected in their former continent-wide distribution, with biomass patterns responding primarily to rainfall at our modeling resolution (36). Surface-water availability is a key determinant of the distribution of this wide-ranging but water-dependent species

Fig. 2. HFT classifications. Vertical color bands with the trait boxplots (left) match the boxes bounding the HFT descriptions (right). Dietary classifications follow (54): obligate grazer (>90% monocots, not variable), variable grazer (60 to 90% monocots, variable), browser-grazer intermediate (30 to 70% dicots and monocots, <20% fruits), generalist (>20% of all food types), browser (>70% dicots), and frugivore (>70% fruits, few or no monocots). Paragon species are close to the centroid of the HFT grouping, and distinctive species are furthest from other HFT groupings.

Fig. 3. Total and HFT biomass. (**A** to **F**) Species-level biomass estimates (kg/km²) were combined to reconstruct total and HFT biomass surfaces ~1000 years ago. In each panel, the darkest colors correspond to the maximum biomass in the given range.

(*40*), but spatial data sets of the requisite detail are not yet available at the continental scale.

HFT classification

We identified five HFTs (Fig. 2 and figs. S4 and S5), with each of the five traits contributing significantly to their delimitation (table S5). Small nonsocial browser species form the largest grouping (35 species) and are selective foragers that can meet their water requirements from their high-quality food sources. This group includes species ranging in habitat from the rainforest (e.g., forest duikers) to the desert (e.g., dik-diks). The medium-sized social mixed-diet group (18 species) tends to consist of species from drier, seasonal environments (e.g., the springbok, Thomson's gazelle, and Grant's gazelle), many of which will switch from selective utilization of new grass or forb growth during the wet season to a browse-dominated diet in the dry season. Eight large-browser species group together (e.g., the greater kudu and giraffe) and are larger, more social, and more water-dependent than the small nonsocial browser group. Water-dependent grazing ruminant species form a cluster of 17 species, many of which are also highly social (e.g., the common wildebeest). Most floodplain-associated species are included in the water-dependent grazer group (e.g., Nile, red, and black lechwes; the puku; and the sitatunga). The final grouping consists of all 14 nonruminant species, including elephants. Aside from the importance of gut type in delimiting this group, these species also tend to be large and

water-dependent, and most incorporate both grass and browse plants in their diet. A full list of species traits and functional type classifications is provided in table S1.
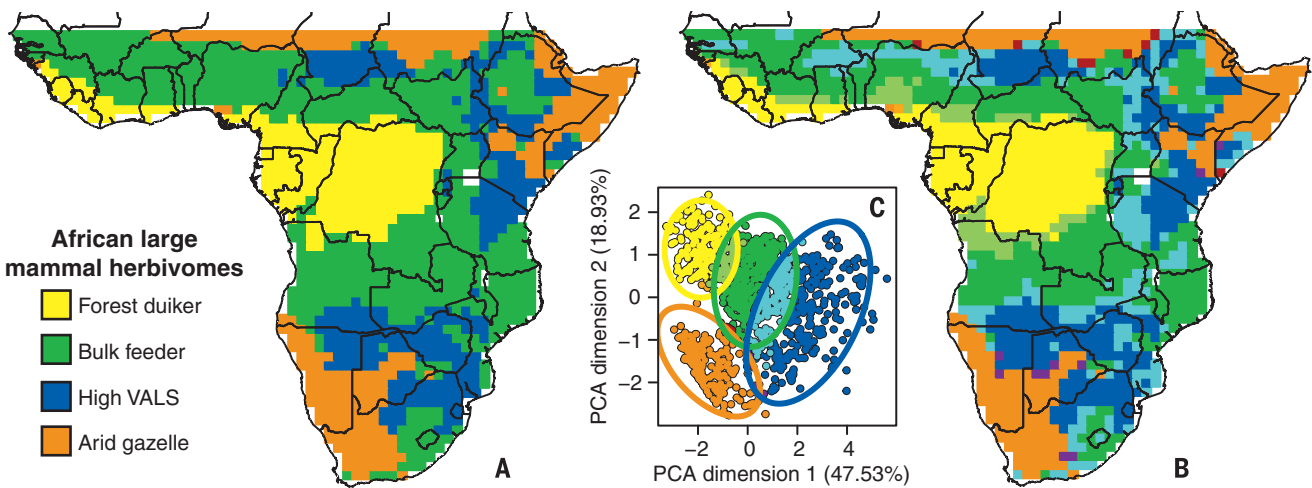
HFT biomass

Combining species-level biomass surfaces by their HFT classification reveals distinct patterns in their relative biomass (Fig. 3). Small nonsocial browsers (Fig. 3B) occur at their highest densities in the forested regions of tropical Africa and display little high-density overlap with either medium-sized social mixed-diet (Fig. 3C) or water-dependent grazer species (Fig. 3E). Medium-sized social mixed-diet species are the only group with relatively high biomass in the western parts of southern Africa and are of perhaps unexpectedly low abundance in open habitats in West Africa. Large browsers (Fig. 3D) and water-dependent grazers species are widely spread in open grassy habitats across the continent, although large browsers are more prominent in the horn of Africa. These patterns (Fig. 3, B to E), however, are overwhelmed by the dominance of nonruminant species (Fig. 3F), which almost exclusively determine patterns in the total biomass of African large mammal herbivores (Fig. 3A).

Classification of large mammal herbivomes

We identified four African large mammal herbivomes (Fig. 4) from our cluster analysis of 1° grid squares, characterized by their total and HFT biomasses (i.e., the surfaces in Fig. 3; figs.

S6 and S7; and table S6). The clearest association between an herbivome and a single HFT is the classification of the forested tropical regions as the "forest duiker herbivome," which closely matches the area of high biomass of small nonsocial browsers (Figs. 3B and 5B). The "arid gazelle herbivome" comprises arid southwestern Africa, the horn of Africa, and the northern parts of the Sahel and has the lowest total herbivore biomass (Fig. 5A). Medium-sized social mixed-diet species are the only HFT to have a significant positive association with this herbivome, but large parts of East Africa with high total biomass and medium-sized social mixed-diet species biomass are not included in this herbivome (Fig. 5). The lack of perfect mapping between HFTs and herbivomes is expected. By analogy, grass and trees occur in forest, savanna, and desert biomes; it is the relative abundance of functional types that is important in recognizing the biome. The arid gazelle herbivome is well resolved at the 1° grid square resolution (Fig. 4B), with very little clustering uncertainty at the 95% level (Fig. 4C). The "bulk feeder herbivome" has the largest total area (Fig. 4A), but this decreases substantially when classification uncertainty is recognized (Fig. 4B). The core distribution of this herbivome comprises two east-west bands at about 10°N and 10°S and also includes the South African Highveld and Ethiopian Highlands. High relative abundances of nonruminant and water-dependent grazer species characterize the bulk feeder herbivome (Fig. 5),

Fig. 4. African large mammal herbivomes. Herbivomes were classified by cluster analysis of total and HFT biomass estimates for each 1° grid square. Grid-square herbivome classifications are shown (**A**) without and (**B**) with classification uncertainty, as determined by (**C**) overlap of 95% confidence ellipses constructed around the mean herbivome position on dimensions 1 and 2 of the principal components analysis. Colors in (B) correspond with those in (C) (purple, arid gazelle–high VALS overlap; dark red, arid gazelle–bulk feeder overlap; orange, arid gazelle–forest duiker overlap; light blue, bulk feeder–high VALS overlap; light green, bulk feeder–forest duiker overlap).
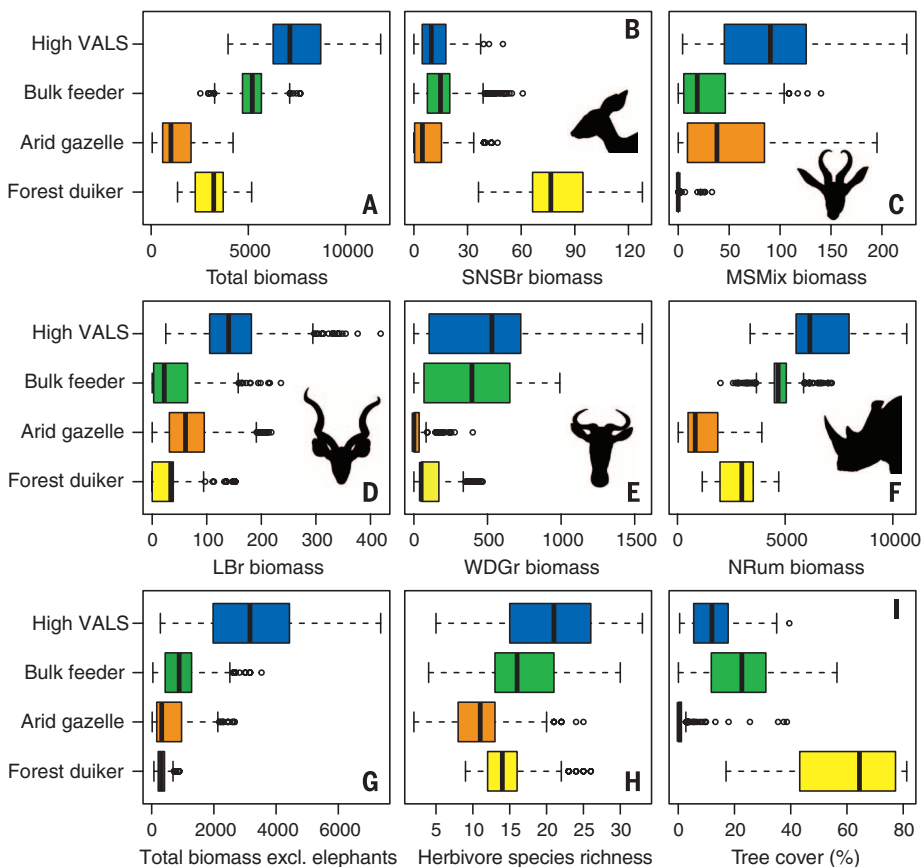
Fig. 5. Characteristics of large mammal herbivomes. (**A**) Total biomass estimates for all 92 species assessed. (**B** to **F**) HFT biomass estimates. (**G**) Total biomass with elephant biomass excluded. (**H**) Herbivore species richness per 1° grid square. (**I**) Percentage of tree cover from (*55*). All herbivore biomass estimates are in kg/km².

which has a high and elephant-dominated total biomass (Fig. 5, A versus G, and fig. S3). The final grouping is the "high VALS herbivome"

(high variety and abundance of larger species), so named because of its positive association with, and high biomass of, each of the four larger-sized

HFTs. This herbivome showcases the diversity of African savanna large mammals (Fig. 5H) and is home to many of East and southern Africa's world-renowned protected areas (e.g., the Masai Mara National Reserve and the Serengeti, Chobe, and Kruger National Parks). It is somewhat patchily distributed across the continent and largely absent from West Africa. The high VALS herbivome differs from the bulk feeder herbivome, which dominates West African savannas, by having a high proportion of large-browser and medium-sized social mixed-diet species (Fig. 5, C and D) and a lower proportion of elephants in the total biomass (Fig. 5, A versus G). Heterogeneity in soil and water distribution at scales smaller than the study resolution probably accounts for the large area of classification uncertainty between these two herbivomes (Fig. 4, B and C).

Environmental correlates

MAR distinguishes the four herbivomes (Fig. 6), with the forest duiker and arid gazelle herbivomes being the wettest and driest, respectively, and the bulk feeder herbivome being wetter than the high VALS herbivome. Mean annual temperature has little discriminatory power (Fig. 6A). Soil nutrient availability separates the bulk feeder and high VALS herbivomes (Fig. 6B), which correspond roughly to the respective distributions of nutrient-poor and nutrient-rich savannas in East and southern Africa (*41*). The bulk feeder herbivome is typified by low-nutrient soils, often associated with high rates of soil leaching in wetter regions. A combination of high rainfall and low nutrients produces a tall grass layer with high C:N stems to provide the structural support to successfully compete for light. Cold winters in the high-lying and wetter regions of South Africa and Ethiopia will also result in a high biomass of cured grass of low forage quality
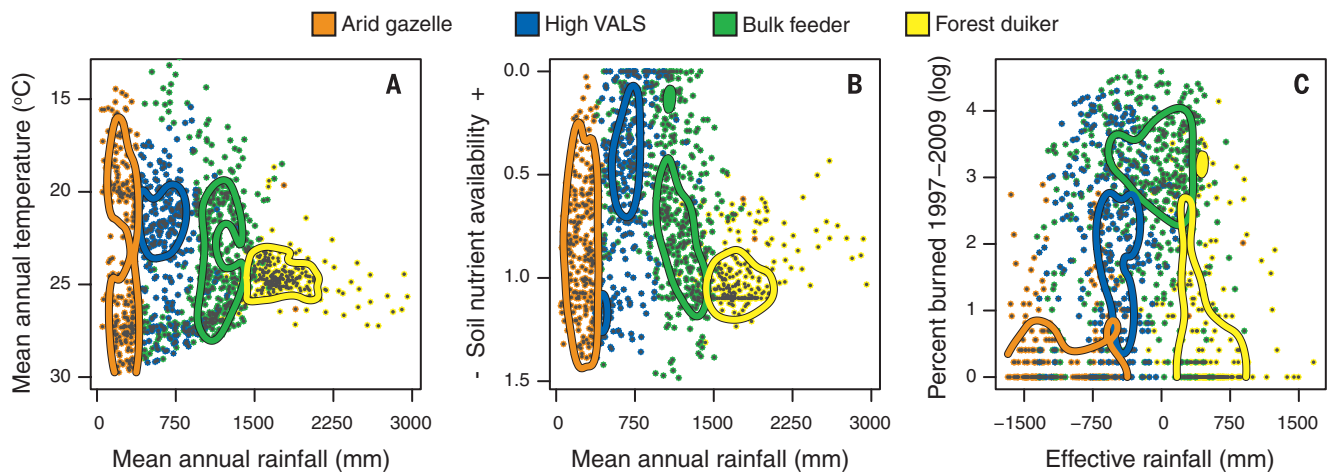
Fig. 6. Herbivomes in environmental space. (**A**) Whittaker plot, as traditionally used to distinguish vegetation biomes (*27*). (**B**) Replacement of mean annual temperature with the natural log of the soil nutrient availability index from the FAO Harmonized World Soils Database (smaller numbers reflect higher nutrient statuses). (**C**) An index of fire activity derived from the Global Fire Emissions Database, shown against effective rainfall (MAR minus potential evapotranspiration). Lines show the 90th quantile of density of unambiguously classified points for each herbivome.

in the winter dry season. Consequently, greater grass fuel loads make the bulk feeder herbivome more fire-prone than the high VALS herbivome (Fig. 6C), and the low-quality grazing necessitates larger body sizes with longer gut passage times to allow for digestion and nutrient extraction (*42*). At similar body sizes, nonruminant gut systems are also better suited to using high-abundance, low-quality resources than ruminant gut systems are, because their less efficient but higher-throughput digestive strategy optimizes nutrient intake rates when forage quantity is not limiting (*43*). The bulk feeder herbivome corresponds to the higher wildlife densities relative to livestock densities above 1000 mm MAR (Fig. 1), suggesting that the full set of species-trait combinations typical of this herbivome is not present in domesticated livestock. Tree cover (Fig. 5I) correlates with the rainfall of each herbivome. Water constraints (Fig. 6C) probably account for the higher tree cover in the bulk feeder herbivome than in the high VALS herbivome (*44*), yet both have the climate potential to produce closed woody canopies (*2, 27*). This suggests that consumer control determines vegetation structure and composition in these herbivomes (*45*), with the role of large mammal herbivory probably increasing as fire becomes less prevalent in the high VALS herbivome (Fig. 6C). The correlation of the high VALS herbivome with low-fire, high-nutrient regions supports long-held theories on the relative importance of fire versus herbivory as consumers in arid and mesic savannas in Africa (*41*).

Implications

Global maps of herbivory are still unobtainable, but quantitative data on large mammal herbivores in Africa will substantially bolster studies seeking to understand their role in driving biome distributions (*4*) and controlling vegetation structure (*16, 17, 46, 47*), as well as how they function as evolutionary and ecological drivers of community assembly (*1, 48*). Furthermore, such data

open the door to understanding the cascading effects of continental-scale trophic downgrading due to the loss of apex predators and other megafauna (*23*). This is of particular relevance, given the growing awareness of the crucial role of biotic interactions in shaping both current and paleoecosystem dynamics, and thus in informing forecasts of species, community, and ecosystem responses to climate change (*24, 25, 49*). Our findings also bring rangeland ecology under new scrutiny, because the replacement of wild herbivores by livestock, with the latter's reduced set of functional traits, might confront regional floras with a novel combination or biomass of HFTs and could expand the scope for fire as a management tool in, for example, the bulk feeder herbivome. Our HFT classifications offer a formal description of the intuitive differences among African herbivores and should considerably facilitate current efforts to include herbivores in DGVMs (*38*). Further exploration of the potential for herbivores to shape vegetation patterns at large scales, which will require estimates of herbivore biomass, should improve our ability to predict the consequences of re-wilding projects (*50, 51*) and the naturalization of novel herbivore groups for ecosystems (*52, 53*). The African continent provides the best example of a near-intact megafaunal assemblage that resembles conditions before the Anthropocene. Extending the herbivome concept beyond Africa's tropical to subtropical ecosystems is likely to reveal a more important role for temperature in delimiting new herbivomes associated with temperate and polar systems, with traits such as the ability to store large fat reserves being important to identifying additional HFTs. Recent research on the consequences of megafaunal extinctions has had to grapple with the relative importance of herbivory and fire (*20, 21*). Integrating the extent and selectivity of vegetation consumption by herbivores and fire at large scales will allow exploration of their respective and synergistic roles in

shaping past, current, and future global vegetation patterns and Earth system feedbacks.

REFERENCES AND NOTES

1. W. J. Bond, J. E. Keeley, *Trends Ecol. Evol.* **20**, 387–394 (2005).
2. W. J. Bond, F. I. Woodward, G. F. Midgley, *New Phytol.* **165**, 525–538 (2005).
3. B. P. Murphy *et al.*, *J. Biogeogr.* **40**, 1048–1058 (2013).
4. C. E. R. Lehmann *et al.*, *Science* **343**, 548–552 (2014).
5. E. Dwyer, S. Pinnock, J. Gregoire, J. M. C. Pereira, *Int. J. Remote Sens.* **21**, 1289–1302 (2000).
6. G. van der Werf *et al.*, *Atmos. Chem. Phys. Discuss.* **10**, 16153–16230 (2010).
7. W. J. Bond, G. F. Midgley, F. I. Woodward, M. T. Hoffman, R. M. Cowling, *S. Afr. J. Bot.* **69**, 79–91 (2003).
8. D. M. J. S. Bowman *et al.*, *Science* **324**, 481–484 (2009).
9. S. Scheiter, S. I. Higgins, *Glob. Change Biol.* **15**, 2224–2246 (2009).
10. M. Martin Calvo, I. C. Prentice, *New Phytol.* **208**, 987–994 (2015).
11. D. J. Beerling, C. P. Osborne, *Glob. Change Biol.* **12**, 2023–2031 (2006).
12. W. J. Bond, A. C. Scott, *New Phytol.* **188**, 1137–1150 (2010).
13. S. Scheiter *et al.*, *New Phytol.* **195**, 653–666 (2012).
14. N. Owen-Smith, *Megaherbivores* (Cambridge Univ. Press, Cambridge, 1988).
15. S. A. Zimov *et al.*, *Am. Nat.* **146**, 765–794 (1995).
16. G. P. Asner *et al.*, *Proc. Natl. Acad. Sci. U.S.A.* **106**, 4947–4952 (2009).
17. M. Sankaran, D. J. Augustine, J. Ratnam, *J. Ecol.* **101**, 1389–1399 (2013).
18. F. Keesing, T. P. Young, *Bioscience* **64**, 487–495 (2014).
19. D. A. Burney, T. F. Flannery, *Trends Ecol. Evol.* **20**, 395–401 (2005).
20. J. L. Gill, J. W. Williams, S. T. Jackson, K. B. Lininger, G. S. Robinson, *Science* **326**, 1100–1103 (2009).
21. S. Rule *et al.*, *Science* **335**, 1483–1486 (2012).
22. J. L. Gill, *New Phytol.* **201**, 1163–1169 (2014).
23. J. A. Estes *et al.*, *Science* **333**, 301–306 (2011).
24. J. L. Blois, P. L. Zarnetske, M. C. Fitzpatrick, S. Finnegan, *Science* **341**, 499–504 (2013).
25. M. S. Wisz *et al.*, *Biol. Rev. Camb. Philos. Soc.* **88**, 15–30 (2013).
26. L. R. Holdridge, *Science* **105**, 367–368 (1947).
27. R. Whittaker, *Communities and Ecosystems* (MacMillan, New York, ed. 2, 1975).
28. S. Lavorel, S. McIntyre, J. Landsberg, T. D. A. Forbes, *Trends Ecol. Evol.* **12**, 474–478 (1997).
29. S. Díaz, M. Cabido, *Trends Ecol. Evol.* **16**, 646–655 (2001).
30. F. I. Woodward, M. R. Lomas, C. K. Kelly, *Philos. Trans. R. Soc. London Ser. B* **359**, 1465–1476 (2004).

31. S. Archibald, C. E. R. Lehmann, J. L. Gómez-Dans, R. A. Bradstock, *Proc. Natl. Acad. Sci. U.S.A.* **110**, 6442–6447 (2013).
32. Materials and methods are available as supplementary materials on *Science* Online.
33. R. East, *Afr. J. Ecol.* **22**, 245–270 (1984).
34. M. J. Coe, D. H. Cumming, J. Phillipson, *Oecologia* **22**, 341–354 (1976).
35. H. Fritz, P. Duncan, *Proc. Biol. Sci.* **256**, 77–82 (1994).
36. H. Fritz, P. Duncan, I. J. Gordon, A. W. Illius, *Oecologia* **131**, 620–625 (2002).
37. H. Olff, M. E. Ritchie, H. H. T. Prins, *Nature* **415**, 901–904 (2002).
38. A. Pachzelt, A. Rammig, S. Higgins, T. Hickler, *Ecol. Modell.* **263**, 92–102 (2013).
39. M. Oesterheld, O. E. Sala, S. J. McNaughton, *Nature* **356**, 234–236 (1992).
40. S. Chamaillé-Jammes, M. Valeix, H. Fritz, *J. Appl. Ecol.* **44**, 625–633 (2007).
41. R. J. Scholes, B. H. Walker, *An African Savanna: Synthesis of the Nylsvley Study* (Cambridge Univ. Press, Cambridge, 1993).
42. M. W. Demment, P. J. Van Soest, *Am. Nat.* **125**, 641–672 (1985).
43. A. W. Illius, I. J. Gordon, *Oecologia* **89**, 428–434 (1992).
44. M. Sankaran *et al.*, *Nature* **438**, 846–849 (2005).
45. W. J. Bond, *J. Veg. Sci.* **16**, 261–266 (2005).
46. G. Bucini, N. P. Hanan, *Glob. Ecol. Biogeogr.* **16**, 593–605 (2007).
47. M. Sankaran, J. Ratnam, N. P. Hanan, *Glob. Ecol. Biogeogr.* **17**, 236–245 (2008).
48. T. Charles-Dominique, A. C. Staver, G. F. Midgley, W. J. Bond, *S. Afr. J. Bot.* (2015).
49. P. L. Zarnetske, D. K. Skelly, M. C. Urban, *Science* **336**, 1516–1518 (2012).
50. J. Donlan, *Nature* **436**, 913–914 (2005).
51. S. A. Zimov, *Science* **308**, 796–798 (2005).
52. S. Legge, M. S. Kennedy, R. Lloyd, S. A. Murphy, A. Fisher, *Aust. Ecol.* **36**, 791–799 (2011).
53. J. C. Z. Woinarski, A. A. Burbidge, P. L. Harrison, *Proc. Natl. Acad. Sci. U.S.A.* **112**, 4531–4540 (2015).
54. M. Gagnon, A. E. Chew, *J. Mammal.* **81**, 490–511 (2000).
55. M. C. Hansen *et al.*, *Earth Interact.* **7**, 1–15 (2003).

REPORTS

PHOTOPHYSICS

Semiconductor interfacial carrier dynamics via photoinduced electric fields

Ye Yang,[1]*† Jing Gu,[1]† James L. Young,[1,2] Elisa M. Miller,[1] John A. Turner,[1] Nathan R. Neale,[1] Matthew C. Beard[1]*

Solar photoconversion in semiconductors is driven by charge separation at the interface of the semiconductor and contacting layers. Here we demonstrate that time-resolved photoinduced reflectance from a semiconductor captures interfacial carrier dynamics. We applied this transient photoreflectance method to study charge transfer at p-type gallium-indium phosphide (p-GaInP$_2$) interfaces critically important to solar-driven water splitting. We monitored the formation and decay of transient electric fields that form upon photoexcitation within bare p-GaInP$_2$, p-GaInP$_2$/platinum (Pt), and p-GaInP$_2$/amorphous titania (TiO$_2$) interfaces. The data show that a field at both the p-GaInP$_2$/Pt and p-GaInP$_2$/TiO$_2$ interfaces drives charge separation. Additionally, the charge recombination rate at the p-GaInP$_2$/TiO$_2$ interface is greatly reduced owing to its p-n nature, compared with the Schottky nature of the p-GaInP$_2$/Pt interface.

Semiconductor photoelectrodes used in photo-electrochemical (PEC) cells directly convert sunlight into stored chemical potential (*1–5*). Junctions that form between a semiconductor and a contact layer are the key to charge separation that drives photoconversion processes. Equilibration of chemical potential at such junctions creates an internal electric field (referred to as the built-in field) and establishes a region where mobile charges are driven away

known as the depletion region. Absorption of light within the depletion region results in charge separation by the built-in field. As a result, photogenerated electrons (holes) transfer across the interface to participate in a reduction (oxidation) reaction and holes (electrons) are transported to the counter electrode via the external circuit for the oxidation (reduction) reaction. However, the photocarriers can also recombine across the same interface, and such recombination reduces the energy conversion efficiency. Thus, the carrier dynamics—charge separation and recombination across junctions—represent a key determining factor in the PEC performance. Time-resolved spectroscopies are normally employed to study ultrafast carrier dynamics in semiconductors (*6–8*) and semicon-

ductor nanostructures (*9–12*) by probing the kinetics of the spectral features of initial and/or final states. Time-resolved surface-sensitive spectroscopy also has been exploited to study the semiconductor surface dynamics (*13*). However, isolating spectral signatures and/or the carrier dynamics that are specific to junctions—often strongly affecting subsurface depths of tens of nanometers such as in photoelectrodes—is challenging.

Here, we introduce transient photoreflectance (TPR) spectroscopy to probe the dynamics of the transient electric field (ΔF) caused by charge separation and recombination at a junction of interest. In the TPR method, the change in reflectance (ΔR) of a broadband probe from a specific interface is monitored as a function of pump-probe delay (Fig. 1). We applied TPR to study the p-type gallium-indium-phosphide (p-GaInP$_2$) photoelectrode system, a well-known photocathode for light-driven hydrogen evolution (*3*, *14*). We compare TPR spectral and dynamical signatures of bare p-GaInP$_2$ with p-GaInP$_2$/platinum (Pt) and p-GaInP$_2$/amorphous titania (TiO$_2$) photoelectrodes. We demonstrate that TPR can extract the dynamics of ΔF upon photoexcitation, as well as the magnitude of the built-in field (F) in these junctions.

TPR spectroscopy is a pump-probe technique (Fig. 1) and in our experiment, the temporal response was ~150 fs. The pump photon energy of 3.1 eV corresponded to a pump penetration depth of 29 nm according to the absorption coefficient (fig. S1). The probe was a white-light continuum with photon energy $\hbar\omega$ between 1.55 and 2.40 eV, corresponding to effective detection depths between 18 to 10 nm, as approximated by $\lambda/4\pi n$ (where λ is wavelength and n is refractive index). The photocarrier density was calculated from the absorption coefficient and pump photon flux. The pump and probe beams were overlapped at the electrode surface, and the reflected probe directed to a spectrometer for reflectance spectrum (R) detection. The photoelectrode consisted of a ~1-μm-thick top layer of p-GaInP$_2$ epitaxially grown on a GaAs substrate. The absorption coefficient and refractive index of p-GaInP$_2$ were determined

[1]National Renewable Energy Laboratory, Chemistry and Nanoscience Center, Golden, CO, 80401, USA. [2]Material Science and Engineering Program, University of Colorado, Boulder, CO, 80309, USA.
*Corresponding author. E-mail: ye.yang@nrel.gov (Y.Y); matt.beard@nrel.gov (M.C.B) †These authors contributed equally to this work.

Science

▲▲AAAS

A continent-wide assessment of the form and intensity of large mammal herbivory in Africa

Gareth P. Hempson *et al.*

Science **350**, 1056 (2015);
DOI: 10.1126/science.aac7978